Nuclear Engineering and Technology 54 (2022) 2120–2134

Contents lists available at ScienceDirect

Nuclear Engineering and Technology

journal homepage: www.elsevier.com/locate/net

Original Article

Numerical evaluation of hypothetical core disruptive accident in full-scale model of sodium-cooled fast reactor

Zhihong Guo [a, c, d], Xiaodong Chen [a, *], Guoqing Hu [b]

[a] School of Aerospace Engineering, Beijing Institute of Technology, Beijing, 100081, China
[b] Department of Engineering Mechanics, Zhejiang University, Hangzhou, 310027, China
[c] The State Key Laboratory of Nonlinear Mechanics, Institute of Mechanics, Chinese Academy of Sciences, Beijing, 100190, China
[d] School of Engineering Science, University of Chinese Academy of Sciences, Beijing, 100049, China

ARTICLE INFO

Article history:
Received 10 August 2021
Received in revised form
14 November 2021
Accepted 5 December 2021
Available online 10 December 2021

Keywords:
Hypothetical core destructive accidents
Sodium-cooled fast reactors
Multi-material arbitrary Lagrangian-Eulerian (MMALE) method
Fluid-structure interactions

ABSTRACT

A hypothetical core destructive accident (HCDA) has received widespread attention as one of the most serious accidents in sodium-cooled fast reactors. This study combined recent advantages in numerical methods to realize realistic modeling of the complex fluid–structure interactions during HCDAs in a full-scale sodium-cooled fast reactor. The multi-material arbitrary Lagrangian–Eulerian method is used to describe the fluid–structure interactions inside the container. Both the structural deformations and plug rises occurring during HCDAs are evaluated. Two levels of expansion energy are considered with two different reactor models. The simulation results show that the container remains intact during an accident with small deformations. The plug on the top of the container rises to an acceptable level after the sealing between the it and its support is destroyed. The methodology established in this study provides a reliable approach for evaluating the safety feature of a container design.

1. Introduction

A hypothetical core disruptive accident (HCDA) is the most severe accident in a sodium-cooled fast reactor, which may cause radioactive release [1]. An HCDA is generally divided into three stages after the core melt: initial, transition, and expansion stages [2]. The initial stage determines the initial conditions of the core disintegration transition: reactor power, core temperature distribution, pressure distribution, reactivity state, and introduction of significant energy is introduced into the transformation process. In the transition stage, evaluating the energy level during critical accidents is significant. The expansion stage after the core disintegrates is mainly caused by the thermal energy generation in the crucial process and is converted into mechanical energy, which may cause damage to the reactor boundary [3–6]. Owing to the different accident conditions in each stage, there may be two different consequences. One is the generation of bubbles and expansion after the core is damaged, which causes deformation of the reactor and leakage of the radioactive materials. The other is that the core melts to cause the bottom components of the reactor to melt [7,8]. This study focuses on the first effect.

From the 1970s to the 1980s, the United States and Europe led in the research on the evaluation of the integrity of liquid-metal fast breeder reactors (LMFBRs) [9]. As one of the earliest countries in Asia to develop nuclear power plants, Japan has increased its analysis of Japan sodium-cooled fast reactor responses to serious accidents since the Fukushima Daiichi nuclear disaster [10]. Because the internal structure of a fast reactor is very complex and a fast reactor is typically large, the research methods are mainly classified into two types [11]. One type uses a simplified small model to represent a reactor and conducts simulation research by experiments [12–14]. For example, the French MARA program built a 1/30 scale model based on the Superphenix reactor and conducted ten experimental tests to gradually increase the complexity of the internal deformable structure. The United States also built a 1/30 scale model based on a typical demonstration-size loop-type LMFBR to investigate the physical mechanics of bubble expansion in an HCDA [15]. The second method type is to develop a computer code and verify it against experiments. Many calculation programs are available for HCDA simulation. The finite-difference program, SEURBNUK, can easily deal with the fluid–structure coupling problem and has been combined with the finite element program, EURDYN, considering the memory structure calculation [16,17]. The

* Corresponding author.
E-mail address: xiaodong.chen@bit.edu.cn (X. Chen).

https://doi.org/10.1016/j.net.2021.12.005

finite-difference program, ASTARTE, based on a Lagrangian description can describe a thin-shell structure having a compressible fluid and a simple geometry [18]. The French two-dimensional axisymmetric program, CASSIOPEE, uses the arbitrary Lagrangian–Eulerian (ALE) method, which represents an incompressible fluid by the Euler method and a thin-shell structure by the Lagrangian method [19]. The Lagrangian program, SIRIUS, uses the finite-difference method to describe fluids and thick structures and the finite element method to describe thin-shell structures [20]. A French team used the ALE transient finite element program, CASTEM-PLEXUS, to predict an actual reactor operation and conducted axisymmetric simulations of the MARA series of experiments [21,22]. A ternary constitutive model of a sodium–bubble–argon interaction was studied using CASTEM-PLEXUS and subsequently verified by the container load and response team (CONT) experimental model. Robbe et al. used the CASTEM-PLEXUS code to estimate the mechanical effects of an HCDA on an LMFBR [23]. The EUROPLEXUS program was developed by combining CASTEM-PLEXUS with PLEXIS-3C to improve fluid–structure coupling [24,25]. Robbe et al. used the EUROPLEXUS code to compute an HCDA in a MARS mock-up and compared the results with previous ones obtained using the CASTEM-PLEXUS code [26]. Recently, Faucher et al. used a hybrid parallel strategy in the EUROPLEXUS code to simulate the fast transient dynamics of fully coupled fluid–structure systems to study an HCDA at the reactor scale [27].

The HCDA numerical calculation programs mentioned above can be classified into three categories, each having its own advantages and disadvantages.

(1) In the Lagrangian formulation, grid nodes are fixed on mass points and move with the object. The advantage is that the coordinates of the boundary points remain unchanged after deformation; therefore, the boundary conditions are easy to deal with. The disadvantage is that a mesh is distorted after a large deformation, and the calculation accuracy is reduced or even diverged. The Lagrangian formulation is commonly used for small deformation problems in solid mechanics. A Lagrangian-type program used for HCDA mechanical analysis is EURDYN.
(2) In the Eulerian formulation, grid nodes are fixed in space and remain unchanged. The advantage is that the grid is not distorted by a large deformation or flow of the object; therefore, it is a common solution for fluid mechanics. The disadvantages are the change in the coordinates of the boundary or interface points after a deformation, difficulty to deal with the boundary conditions and the interface coupling conditions, and inconvenience in dealing with the problem of fluid–structure coupling. Eulerian-type programs used for HCDA mechanical analysis are CASSIOPEE and SEURBNUK.
(3) In the ALE formulation, grid nodes can be moved in any specified manner. If they are specified to move with an object or are fixed in space, the formulation degenerate into the Lagrangian or Eulerian formulation. The ALE formulation has the advantages of both Lagrangian and Eulerian formulations, and is currently the best solution for the problem of fluid–structure coupling. Examples of ALE programs used for HCDA mechanical analysis are CASSIOPEE, PLEXUS-3C, CASTEM-PLEXUS, and EUROPLEXUS. However, most of the above computer codes using the ALE format have some limitations. For example, CASSIOPEE can only use the Euler formulation to process incompressible fluids and the Lagrangian format to process thin shells. The remaining three calculation codes are based on PLEXUS as the prototype, and the main disadvantage is that it is not general and convenient compared with the commonly used LS-DYNA software. With the continuous development of sodium-cooled fast reactors, there is an urgent need for a more accurate and general method to assess the impact of HCDAs.

Accurate evaluation of an HCDA requires consideration of the nonlinear dynamic processes of the structures and fluid systems under high-speed transient loads. An HCDA problem is typically treated as a transient fluid–solid coupling problem involving multiphase fluids and complex structures. Until now, the extensively used method for dealing with this type of three-dimensional high-speed transient process is combining the multiphase ALE method and a fluid–structure coupling algorithm with an explicit dynamic analysis method in the framework of the finite element method [28]. It is quite difficult to consider all three stages in one model. This study focuses on the expansion stage of an HCDA using the commonly validated commercial software, LS-DYNA, to evaluate structural deformations as well as plug rises in a full-scale model.

2. Numerical considerations

2.1. Geometry models

In this study, numerical simulations are conducted based on a prototype of a newly developed sodium-cooled fast reactor by the China Institute of Atomic Energy. Appropriate simplifications are introduced to exclude small details while not affecting the main structures significantly. Geometric models are established in SolidWorks (version 2017, Dassault Systems, French) software using surfaces to represent structures that can be simplified as shells and solid bodies represent the other structures. In a typical reactor design prototype, there is a heat shield outside the core to protect the main container and other components. It is used to weaken the core nuclear radiation and prevent the other structures from being directly irradiated and embrittled. It is generally a cylindrical body formed of one or more layers of stainless steel or boron steel, without space between the layers [29]. Thus, it is simplified as a solid structure in our simulations. Two reactor models, without and with a heat shield, are considered here. Fig. 1 shows the geometries of the two full-scale models: without (Fig. 1a) and with (Fig. 1b) a heat shield.

One of the objectives of this study is to evaluate the rise of the plug at the top of the container. There are three main parts of the plug module: large, middle, and small plugs. The plug module and the main container are connected by breakable seals of a tin–bismuth alloy to represent the real physical process. When the force generated by an explosion is sufficiently large, the plug rises and leakage channels are opened, causing leakage of the protective gas and the liquid sodium. However, leakage channels are complex to model. In addition, their sizes are extremely small to model in a full-sized model. For example, the average size of the leakage channels of the considered reactor is 20 mm, whereas the reactor model established in this study has a height of approximately 10 m and a width of approximately 5 m. Because the structure of the plug in the reactor is complex to model, it is necessary to ensure that the simplification of the plug module does not affect the involved mechanisms when establishing the numerical simulation model. Two different models of the plug are established, as shown in Fig. 2. One is an integral model (Fig. 2a), which considers the plug module as a whole, and the other is a separated model (Fig. 2b), which considers the main structures of the large, middle, and small plugs as well as their interactions. As the gaps between the individual plugs are sealed with the tin–bismuth alloy, the bonding contact type with invalidation is used. The failure criterion is based on the

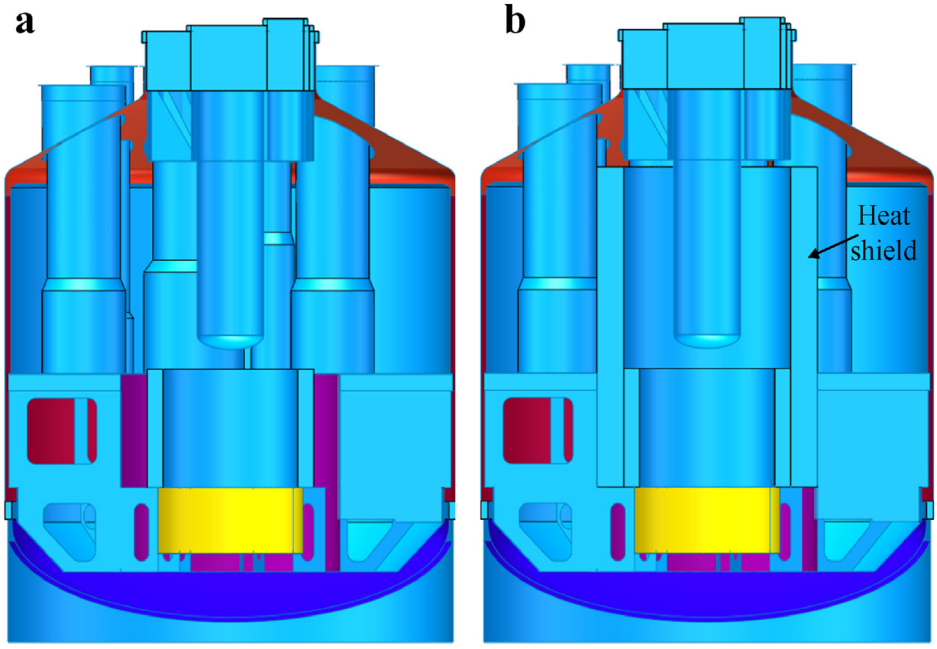

Fig. 1. Geometries of overall models: (a) Model without heat shield and (b) Model with heat shield.

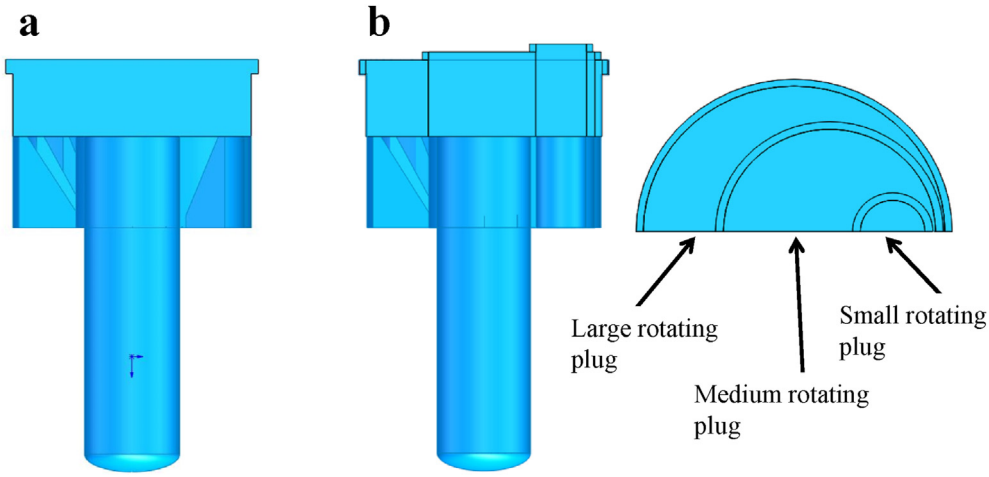

Fig. 2. Geometries of plug models (a) Integral model (b) Separated model.

experimentally estimated maximum shear force that the tin–bismuth alloy can sustain [30]. If the criterion is reached, then the connected components are disconnected.

Subsequently, the entire model is exported into a single geometric file and imported into ANSYS WorkBench (version 18.0, ANSYS, USA) for meshing. The connection between different components is one of the problems that is focused on in this study. If two interconnected mesh nodes need to overlap to achieve force transfer, then the method used in this study is to import different components into DesignModeler and combine the interconnected mesh nodes into one. This approach ensures that the interlinked components in the subsequent meshing use the same mesh nodes. The structures are then meshed in ANSYS Mesh. Fig. 3a shows Lagrangian meshes of different components. The meshes of various components use the same nodes at the joints, which ensures accurate transmission of the stress and strain information of the nodes. Subsequently, the meshes is exported and imported into LS-PrePost (version R11, Livermore Software Technology Corporation, USA). Owing to the complexity of the model, the abovementioned method is unsuitable for the connections between a shell and solid elements. Thus, bonding contacts are established in LS-PrePost to achieve appropriate connections. Fig. 3b shows an example of this type of bonding contact, which is between the plug and the solid elements and the adjusted shells. The green nodes are the nodes attached to the surface of the shell boundary. In addition, as shown in Fig. 3c, the beams inside the lower core support structure are bonded to the shells at the boundary nodes of the beams similarly.

Owing to the symmetry of the studied reactor, one half of the model is considered in our numerical simulation, as shown in Fig. 4a. A structured multi-material ALE (MMALE) mesh with cube elements for fluids is directly created in LS-PrePost. The structured mesh provides higher computational efficiency and precision than an unstructured mesh. Fig. 4b shows that the MMALE mesh overlaps that of the structure. The grid resolutions during simulations

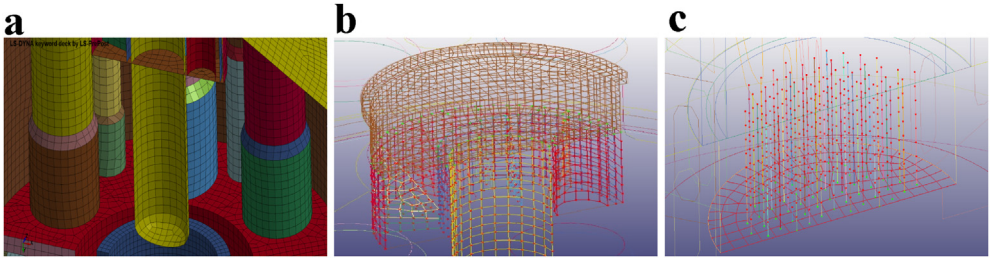

Fig. 3. Connection method between components: (a) Meshes of different components use same nodes at joints, (b) Boundaries of multiple shells are bound to surface set, and green nodes are nodes bound to surface of shell boundary, and (c) Boundary nodes of beams are bound to surface set, and green nodes are bound nodes. (For interpretation of the references to color in this figure legend, the reader is referred to the Web version of this article.)

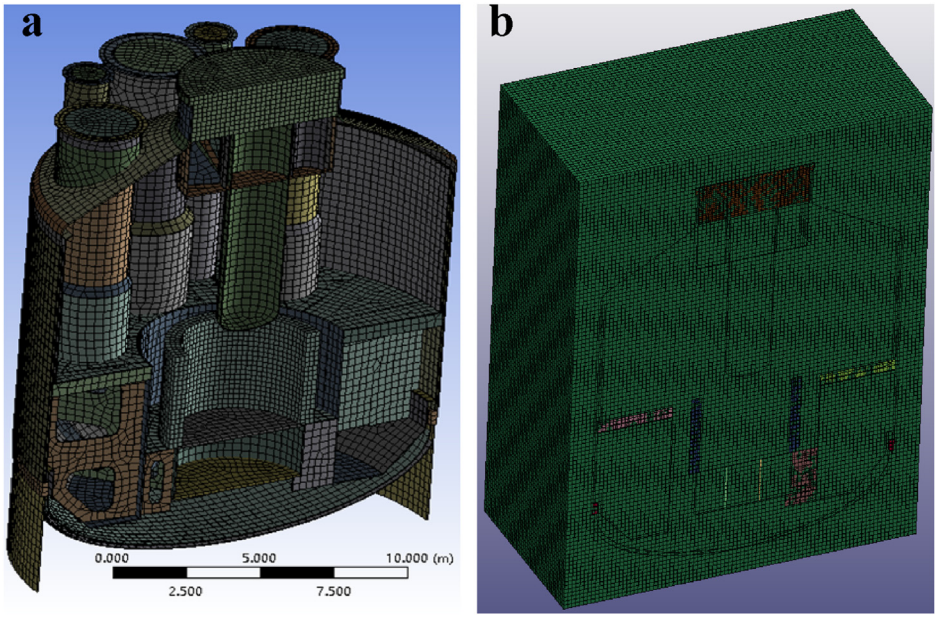

Fig. 4. (a) Meshes of structures of reactor model and (b) Structured MMALE mesh overlap with reactor model.

are determined considering both cost and accuracy. The maximum mesh size is 280 mm for the structures, whereas the grid resolution of the MMALE mesh is 200 mm. This resolution to ensure 10 element across the initial diameter of the gas core. After the model is created, necessary settings can be added or modified in LS-PrePost to complete the simulation files. The simulations are conducted using LS-DYNA (version R11, Livermore Software Technology Corporation, USA) on the engineering simulation cloud computing service platform of Shanghai Supercomputing Technology Co., Ltd. Table 1 shows calculation conditions of simulation cases in this study.

2.2. Numerical methods

Numerical simulations of HCDAs involve flows of the gas core, liquid sodium, protection gas, and ambient air as well as their interactions with each other and solid structures. In this study, the MMALE and Lagrangian methods are selected to describe the fluids and the structures, respectively. Thus, fluids and structures are modeled with separate meshes. Fluid–structure interactions are determined by coupling between the MMALE and Lagrangian meshes.

The MMALE method allows a finite element mesh to move independently of the material flow, and each element in the mesh can contain a mixture of two or more different materials [31]. The total time derivative of a variable f with respect to a reference coordinate can be expressed as [32].

$$\frac{df(\boldsymbol{X},t)}{dt}=\frac{df(\boldsymbol{x},t)}{dt}+(\boldsymbol{u}-\boldsymbol{w})\cdot\nabla f(\boldsymbol{x},t) \tag{2.1}$$

where $\boldsymbol{X}$ is the Lagrangian coordinate, $\boldsymbol{x}$ is the ALE coordinate, $\boldsymbol{u}$ is the particle velocity, and $\boldsymbol{w}$ is the velocity of the reference coordinate or the grid velocity of the ALE grid. Thus, the ALE equations can be derived by substituting the relationship between the total time derivative and the reference configuration time derivative. The equations of the mass, momentum, and energy conservation of a Newtonian fluid in the ALE formulation in the reference domain are expressed in Eqs. (2.2)–(2.4), respectively.

Table 1
Calculation conditions of simulation cases.

Case Number	Heat Shield	Plug Geometry	Energy Level
1	without	Integral	50 MJ
2	without	Integral	100 MJ
3	without	Separated	50 MJ
4	without	Separated	100 MJ
5	with	Separated	100 MJ

$$\frac{\partial \rho}{\partial t}+\rho\nabla\cdot\boldsymbol{u}+(\boldsymbol{u}-\boldsymbol{w})\cdot(\nabla\rho)=0 \tag{2.2}$$

$$\rho\frac{\partial \boldsymbol{u}}{\partial t}+\rho[(\boldsymbol{u}-\boldsymbol{w})\cdot\nabla]\boldsymbol{u}=\nabla\boldsymbol{\sigma}+\boldsymbol{f} \tag{2.3}$$

$$\rho\frac{\partial \mathrm{e}}{\partial t}+[(\boldsymbol{u}-\boldsymbol{w})\cdot\nabla]\rho e=(\boldsymbol{\sigma}:\nabla)\boldsymbol{u}+\boldsymbol{f}\cdot\boldsymbol{u} \tag{2.4}$$

where ρ is the density, $\boldsymbol{f}$ is the inertia force term, e is the internal energy per unit volume, and $\boldsymbol{\sigma}$ is the total Cauchy stress written in Eq. (2.5). The temperature, T, is computed using the average heat capacity, C_v, in Eq. (2.6).

$$\boldsymbol{\sigma}=-p\mathbf{I}+\mu\left[(\nabla\otimes\boldsymbol{u})+(\nabla\otimes\boldsymbol{u})^{T}\right] \tag{2.5}$$

$$\rho e=C_vT \tag{2.6}$$

There are typically two methods for solving the ALE equations [33]. One is the full coupling method; however, one unit can only contain one material. The other is the operator separation method, in which each time step is divided into two stages. The first stage is the Lagrangian phase in which the mesh changes with the material, and the evolutions of the velocity and internal energy due to the actions of the internal and external forces can be calculated. The second stage is the advection phase, in which the transmission of mass, internal energy, and momentum crossing the unit boundary can be calculated; specifically, the deformed mesh of the first stage is remapped to the initial position or any position. In this study, the second method is used to solve the ALE equations. Before the advection phase, an interface tracking algorithm is applied to accurately calculate the material interface of the ALE elements containing multiple materials (liquid sodium, argon, and air). For these elements, the volume fraction, V_f, of each fluid satisfies

$$V_f\leq 1 \tag{2.7}$$

The total stress, $\boldsymbol{\sigma}$, is weighted by the volume fraction, V_f, to obtain the fluid stress fields as follows:

$$\boldsymbol{\sigma}_f=V_f\boldsymbol{\sigma} \tag{2.8}$$

For solids, the structural algorithms satisfy the momentum conservation and the constitutive relations as follows:

$$\frac{\partial \sigma_{ij}}{\partial x_j}+\rho f_i=\rho\frac{d^2u_i}{dx^2} \tag{2.9}$$

$$\boldsymbol{\sigma}=\boldsymbol{\sigma}(D_{ij},\sigma_{ij},\cdots) \tag{2.10}$$

where $D_{ij}=\frac{1}{2}\left(\frac{\partial u_i}{\partial x_j}+\frac{\partial u_j}{\partial x_i}\right)$ is the deformation rate.

The spatial coordinates of any particle in a solid structural unit at any time are $x_i(X,t)=N_Ix_{iI}(t)$, where the structural space is discretized. N_I is the shape function of node I. Thus, the displacement of any point X in the unit is $u_i(X,t)=N_Iu_{iI}(t)$. Similarly, the velocity and acceleration of any point in the unit can be expressed as $\frac{du_i(X,t)}{dx}=N_I\frac{du_{iI}(t)}{dx}$ and $\frac{d^2u_i(X,t)}{dx^2}=N_I\frac{d^2u_{iI}(t)}{dx^2}$, respectively.

In this study, the explicit center difference method is used to perform time integration. In the case of known 0, 1, … ⋯, t_n time step solutions, the solution of the t_{n+1} time step is solved. The general equation of motion is taken as an example, as expressed below [34].

$$M\frac{d^2U(t_n)}{dt^2}=P(t_n)-KU(t_n)-C\frac{dU(t_n)}{dt} \tag{2.11}$$

where U is the displacement matrix, M is the mass matrix, C is the damping matrix, $P(t_n)$ is the external force vector matrix, and K is the stiffness matrix.

LS-DYNA uses the stepwise integration method to solve the general equation of motion and uses the explicit center difference method to replace $KU(t_n)$ in the equation of motion with $H(t_n)-F^{\mathrm{int}}(t_n)$, as expressed in Eq. (2.12).

$$M\frac{d^2U(t_n)}{dt^2}=P(t_n)-F^{\mathrm{int}}(t_n)+H(t_n)-C\frac{dU(t_n)}{dt} \tag{2.12}$$

where $F^{int(t_n)}$ is the internal force vector, whose expression is $F^{int(t_n)}=\sum\int_{\Omega}B^T\sigma_nd\Omega+F^{contact}$, where $\int_{\Omega}B^T\sigma_nd\Omega$ is the equivalent nodal force per unit stress field, B is the displacement matrix, and $F^{contact}$ is the contact force. The internal force of the element is obtained from the divergence of the stress field of the current configuration and $H(t_n)$ is the hourglass resistance.

The mass matrix is shifted to the right-hand side and the acceleration at time t_n is obtained as follows:

$$\frac{d^2U(t_n)}{dt^2}=M^{-1}\left[P(t_n)-F^{\mathrm{int}}(t_n)+H(t_n)-C\frac{dU(t_n)}{dt}\right] \tag{2.13}$$

The velocity and displacement at time t are obtained by Eqs. (2.14) and (2.15).

$$\frac{d^2U\left(t_{n+1/2}\right)}{dt^2}=\frac{d^2U\left(t_{n-1/2}\right)}{dt^2}+\frac{d^2U(t_n)}{dt^2}\Delta t_n \tag{2.14}$$

$$U(t_{n+1})=U(t_n)+\frac{dU\left(t_{n+1/2}\right)}{dt}\Delta t_{n+1/2},\ while\ \Delta t_{n+1/2}=\frac{\Delta t_n+\Delta t_{n+1}}{2} \tag{2.15}$$

Accordingly, the displacement at time t_{n+1} can be obtained, and the geometric configuration at time t_n can be updated to obtain the new geometric configuration of the system at time t_{n+1}. Because the lumped mass matrix, M, is used, the solution of the motion equation is uncoupled. It is unnecessary to integrate the overall stiffness matrix and adopt single central point integration; this significantly saves the storage space and the machine time in the solution process.

As mentioned earlier, the HCDA problem of the sodium-cooled fast reactor considered in this study is complex involving fluid–structure coupling. In this study, structures described by Lagrangian meshes are embedded in fluids mesh described by MMALE meshes to achieve fluid–solid coupling. The penalty function method is used to treat the interaction between fluids and structures. The coupling process is depicted in Fig. 5a, which begins with searching for the presence of intersections between the Lagrangian parts and MMALE parts [35]. If an intersection is detected inside an MMALE element, the position, X_n, of the coupling point shared by the Lagrangian–Eulerian meshes is marked on the interface at time t^n, and subsequently a "penetration vector" d is used to track X_n to obtain the material coupling point at dt. As shown in Fig. 5b, the motion in the period and the penetration distance are calculated, and finally, the "penalty force" (coupling force) is calculated based on the penetration distance at time t^{n+1}. To determine the "coupling force" between the fluid and

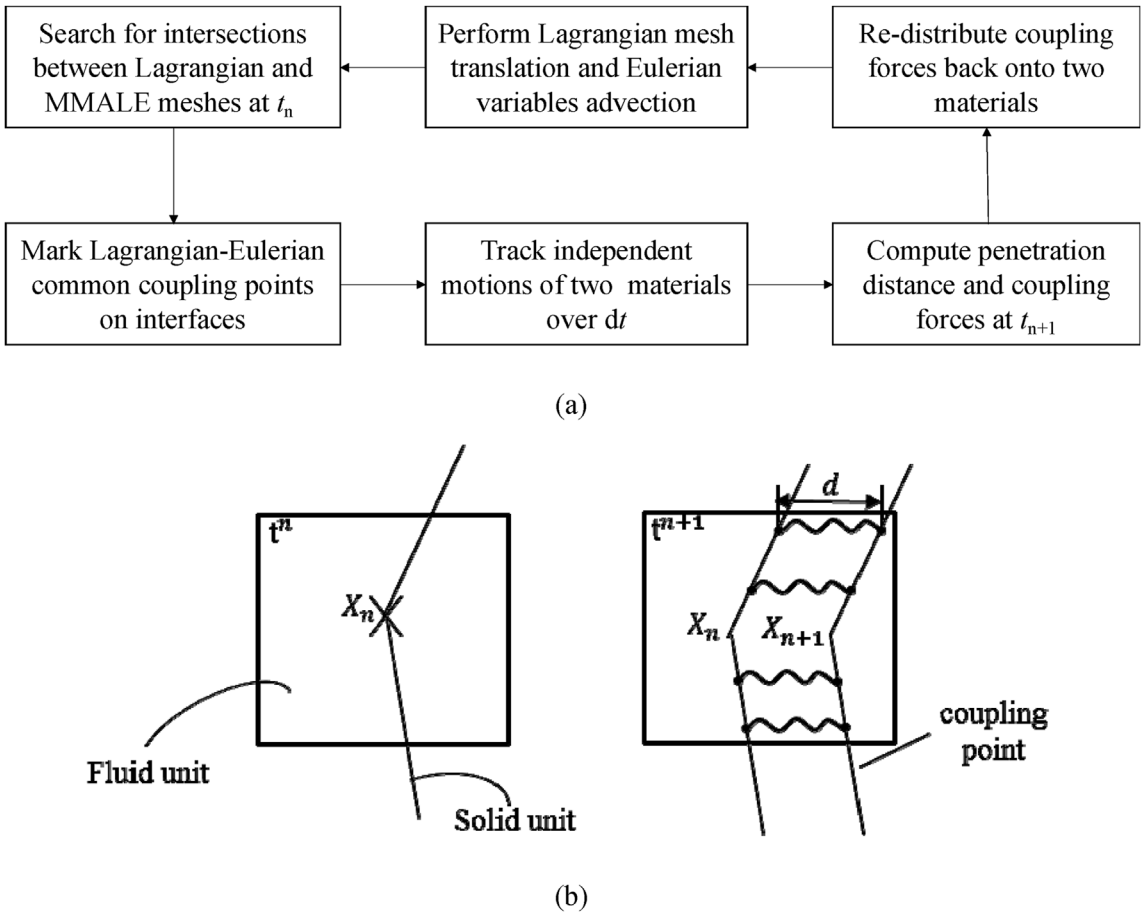

Fig. 5. (a) Flow chart of the detailed coupling process; (b) schematic of penalty-based coupling.

the solid, the function uses additional coupling points in the fluid grid unit. The local density of these points can be adjusted; a high density of coupling points results in an excessive calculation time, whereas a low density causes a distortion leakage effect. Therefore, based on the sufficient guarantee of computing power, this study improves the correctness of the numerical simulation by setting four coupling points. More specifically, the penalty-based coupling algorithm is considered as a spring system, and the penalty force and penetration distance are as follows (2.16) [36]:

$$F = k \cdot D \tag{2.16}$$

where F is the penalty force, k is the spring stiffness, and D is the penetration distance. The penalty force is applied to both the fluid particles and structural nodes. Therefore, to satisfy the force balance, the force acting on the structure, F_s, should be opposite to that on the fluid.

$$F_s = -F \tag{2.17}$$

For the fluid, the coupling force on each node is scaled by the shape function,

$$F_f^i = N_i \cdot F \tag{2.18}$$

where F_f^i is the penalty force on the fluid node.

$$k = \frac{P_f \cdot KA^2}{V} \tag{2.19}$$

where P_f is the penalty factor, K is the bulk modulus of the fluid material, A is the area of the structural segment, and V is the fluid volume.

2.3. Material models

In this study, the material deformation can generally be classified into two types: constant-volume and variable-volume deformation processes. The entire stress tensor is composed of two parts: stress bias and pressure.

$$\sigma'_{ij} = \sigma_{ij} - \sigma_{kk}\delta_{ij},\ \textit{where}\ \sigma_{kk} = [\sigma_{11} + \sigma_{22} + \sigma_{33}] / 3 \propto P \tag{2.20}$$

$$\varepsilon'_{ij} = \varepsilon_{ij} - \varepsilon_{kk}\delta_{ij},\ \textit{where}\ \varepsilon_{kk} = [\varepsilon_{11} + \varepsilon_{22} + \varepsilon_{33}] / 3 \propto \Delta\nu / \nu \tag{2.21}$$

Above, P is the pressure and ν is the viscosity.

For any material, the stress bias and pressure can be used to describe its stress tensor. Thus, for solids, materials with elasto-plastic motion behavior and isotropic hardening are considered. The density, elastic modulus, Poisson's ratio, yield stress, and other parameters of 316H stainless steel at 450 °C are obtained and set based on the literature [37]. For fluids, the constitutive model and the equation of state (EOS) are used to simultaneously describe the properties of the materials. The constitutive model is used to describe the relationship between $\Delta\sigma'_{ij}$ and $\Delta\varepsilon'_{ij}$. The EOS is used to

describe the relationship between ΔP and $\Delta v/v$, i.e., the relationship between the volume deformation and the pressure. The material mode itself provides a constitutive model to describe the deviatoric stress (viscous stress) of the material,

$$\sigma_{ij}^{v} = \sigma_{ij}' = \mu\varepsilon_{ij}' \tag{2.22}$$

The EOS is used to provide pressure behavioral stress components such that they together yield the overall stress tensor of the material.

$$\sigma_{ij} = \sigma_{ij}' + \sigma_{kk}\delta_{ij} = \mu\varepsilon_{ij}' + P\delta_{ij} \tag{2.23}$$

A linear polynomial EOS for liquid sodium is defined to represent the relationship between pressure and volume [38].

$$P = C_0 + C_1\mu + C_2\mu^2 + C_3\mu^3 + \left(C_4 + C_5\mu + C_6\mu^2\right)E \tag{2.24}$$

where the volumetric parameter is $\mu = \rho/\rho_0 - 1$ and E is the internal energy per unit reference volume.

For argon or the gas core, the EOS is $P = C(\varepsilon_V) + \gamma T(\varepsilon_V)E$, where E is the internal energy per unit reference volume and ε_V is the volumetric strain, ln V, where V is the relative volume. C and T are the tabulated points for the function. Table 2 is the EOS table for the gas core. This tabulated EOS model is transformed from the polytropic-type EOS following the CONT case in Ref. [39].

The fluid and the solid are initialized to match the calculation requirements of the MMALE algorithm when the definition of the material properties of the solid and the fluid is completed. In this study, the distribution of fluids, such as air, liquid sodium, argon, and sodium vapor, is initiated based on three characteristics: vessel surface, liquid sodium level, and spherical gas core. The initialization is divided into four steps:

(1) the entire area is initialized to argon;
(2) the fluid below the vertical coordinate of the liquid surface is replaced with liquid sodium based on the position of the liquid sodium level;
(3) the fluid on the surface of the container is replaced with air;
(4) the fluid in the core area is replaced with sodium vapor.

Fig. 6 visually displays the fluid state after initialization and provides the fluid distribution details. Fig. 6a shows the entire fluid area, and Fig. 6b shows the overall fluid distribution after the initialization is complete. Fig.6c–e shows, in order, the fluid distributions after removal of air, argon, and liquid sodium.

It can be found from the material definition and the initialization process that nonphysical penetration is very probable to occur because of the complex contact between the fluids and the solids. When nonphysical penetration occurs, a fluid leaks from the solid boundary abnormally in the location of the nonphysical penetration. By conducting many repeated tests and verifications, this study examined several control methods, identifying a method to control nonphysical penetration, and established the following calculation principles:

(1) the components corresponding to the locations where nonphysical penetration is probable to occur are determined by preliminary calculations;
(2) conventional settings are used for the nonpenetrating parts;
(3) penetration control is applied using multiple algorithms combined for locations where penetration is expected to occur;
(4) the parameters of the penetration control are changed to ensure that nonphysical forces are not introduced.

Two approaches in LS-DYNA are used to suppress or cancel nonphysical penetration. One is to turn on the ILEAK option in the previous step and stretch the new fluid interface by a certain percentage at each time step. The second is to apply a preset suppression pressure within a certain distance of the interface by setting the PFAC option to an increasing straight line. Preliminary simulations show that the parts prone to nonphysical penetration are the plugs and the tapered caps. Conventional settings are used for the nonpenetrating parts. For the interaction of the plug with the liquid sodium, the ILEAK option setting is used to activate the penetration control algorithm. The PFAC option is also used to control the leakage by setting the force of the fluid and the housing as a function of the penetration distance.

Table 2
EOS table for gas core.

eosid	gama	e0	v0	
6	0	32.59	0.011276	
ev1	ev2	ev3	ev4	ev5
0.0	−0.916291	−2.30259	−3.21888	−3.91202
ev6	ev7	ev8	ev9	ev10
−4.60517	−5.116	−5.80914	−6.21461	−6.90776
c1	c2	c3	c4	c5
100.0	198.8	562.3	1118.0	1880.0
c6	c7	c8	c9	c10
3162.0	4639.0	7801.0	10570.0	17780.0
t1	t2	t3	t4	t5
0	0	0	0	0
t6	t7	t8	t9	t10
0	0	0	0	0

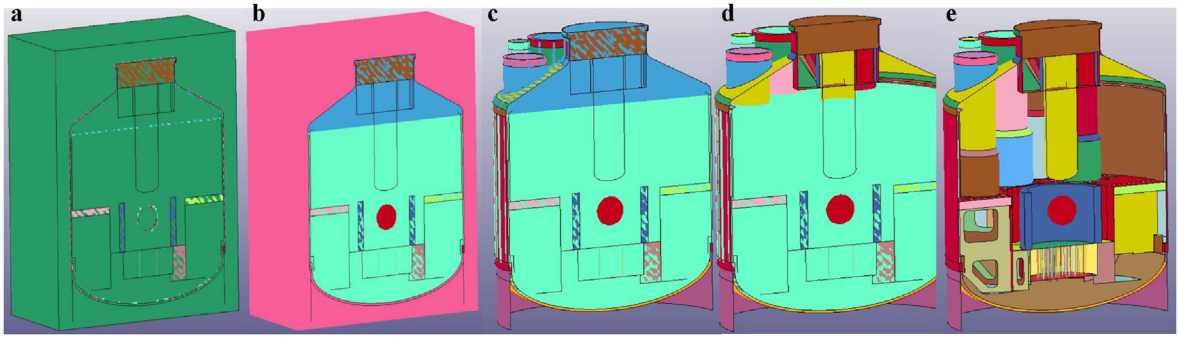

Fig. 6. Fluid distribution details: (a) Entire fluid area, (b) Overall fluid distribution after initialization, (c) Distribution of fluid after removal of air, (d) Distribution of fluid after removal of argon, and (e) Distribution of fluid after removal of liquid sodium. In (c), air, liquid sodium, argon, and sodium vapor are represented in pink, green, blue, and red, respectively. (For interpretation of the references to color in this figure legend, the reader is referred to the Web version of this article.)

3. Results and discussion

3.1. Method validation

Extensive studies on the safety of LMFBRs have led to the commonly accepted conclusion that the initial event leading to an HCDA is improbable, and an HCDA is not considered a design basis accident. Nevertheless, the current safety concept requires determining the impact of such accidents, particularly that on the containers, to assess the risk to the public. Because it is impossible to reproduce HCDAs by experiments, it is necessary to rely on computational prediction based on estimated energy releases. In the late 1980s, the CONT of the Rapid Reactor Coordination Committee of the Commission for the Safety of the European Communities presented recommendations for the submission of container benchmarks simulating HCDAs in full-size LMFBRs by different computer codes. Five organizations participated and tested six computer codes. The test results showed that although the routines used different algorithms and expressions, the difference in the container deformations was between 2% and 12% [39].

In this study, CONT benchmarks are conducted to validate the current methods that will be used for the full simulations. The problem settings are shown in Fig. 7a. After an HCDA occurs, a high-pressure and high-temperature bubble (gas core) is generated in the core region of the LMFBR. The energy release is 600 MJ. Although the CONT case is axisymmetric, a 1/4 domain is established to test the methods in dealing with three-dimensional structures. The structured mesh of the fluids in the main container is constructed, as shown in Fig. 7b. The interface of the three fluids is represented by a grid interface, which ensures the accuracy of the initial fluid spatial distribution. A surface represents the main container and the internal structure, wherein the main container is obtained by copying the boundary of the fluid mesh and the internal structure is treated as a housing embedded with the fluids. Fig. 7c shows the expansion of the gas core. The gas core expands and pushes the liquid sodium upward, which deforms the internal structure and causes the liquid sodium level to rise, thereby compressing the upper protection gas. The pressure wave produced by this process causes the upper part of the container to be plastically deformed, and eventually, the gas core begins to collapse and becomes unstable on the surface. Fig. 7d shows a comparison of the numerical simulation results of this study with the results of other studies [39]. The blue lines refer to the upper and lower limits of the deformed shapes from previous simulations, and the red line represents our numerical simulations. This comparison shows that the results for the CONT examples obtained using the research method of this study are highly consistent with those obtained by the other programs.

3.2. Fluid dynamics

Two levels of the core energies—the mechanical energies released from the accident—are calculated from a modified Bethe–Tait model using the relative parameters of the working conditions of the referenced sodium-cooled fast reactor. The two energy levels are 50 MJ and 100 MJ, which are considered in the numerical simulations to compare the effects of different core energies on the results. The curve of the pressure change at the center of the gas core is shown in Fig. 8. When the core energies are 50 MJ, as shown in Fig. 8a, and 100 MJ, as shown in Fig. 8b, the initial

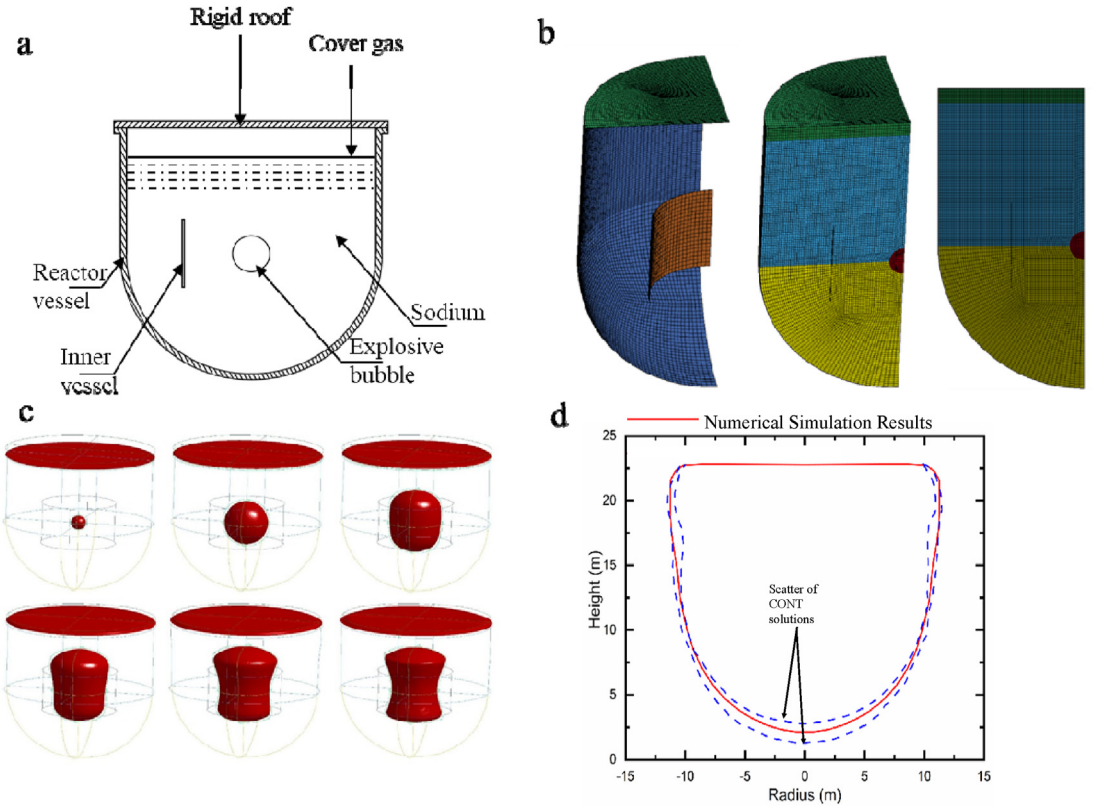

Fig. 7. (a) Model of CONT study, (b) Construction of structural grid of fluids in main container by partition meshing, (c) Simulation results showing interface of gas core and cover gas changes in explosion, (d) Comparison of numerical simulation results of this study with results of other CONT studies. Blue dashed lines refer to upper and lower limits of deformed outer wall shape of container from previous simulations (scatter of CONT solutions), and red line depicts deformed outer wall shape from our numerical simulation. (For interpretation of the references to color in this figure legend, the reader is referred to the Web version of this article.)

pressure values of the gas core center are 2 MPa and 3 MPa, respectively. The gas core pressure rapidly decreases with the development of the HCDA, accompanied by multiple fluctuations, and the final pressure gradually reaches an equilibrium value, which is approximately 0.2 MPa.

Fig. 9a and b shows the expansion dynamics of the gas core without and with the heat shield, respectively, under a core energy of 100 MJ. The continuous development of the HCDA leads to a continuous expansion of the gas core. Simultaneously, it affects the entire reactor and its internal structure, such as the main container and the plug. Under the restriction of the internal structure of the fast reactor, Fig. 9a shows that the gas core first expands outward and impacts the internal structure of the reactor from 0 ms to 300 ms, causing plastic deformation of the reactor cone-top-cover. Subsequently, the gas core contracts inward from 400 ms to 800 ms, and the volume gradually changes. Fig. 9b shows, under the restriction of the heat shield, the gas core rises higher, and expectedly has a stronger impact on the plug. However, the volume of the gas core at the maximum expansion is smaller than that in the case without the heat shield.

Fig. 10a and b further show the flow dynamics of liquid sodium under two cases—without and with the heat shield—respectively. As the gas core expands, sodium is pushed upward. Fig. 10a displays that the interface between sodium and argon raises horizontally.

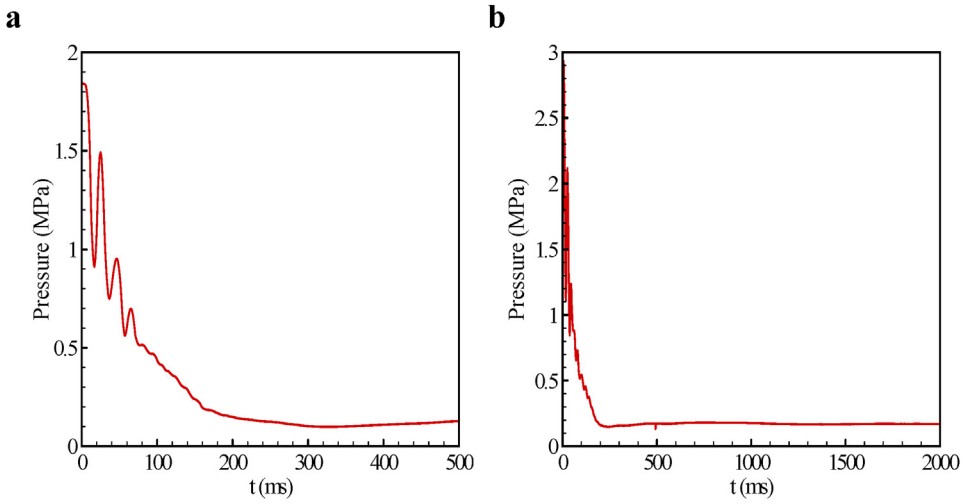

Fig. 8. Curve of pressure change at center of the gas core: (a) 50 MJ and (b) 100 MJ.

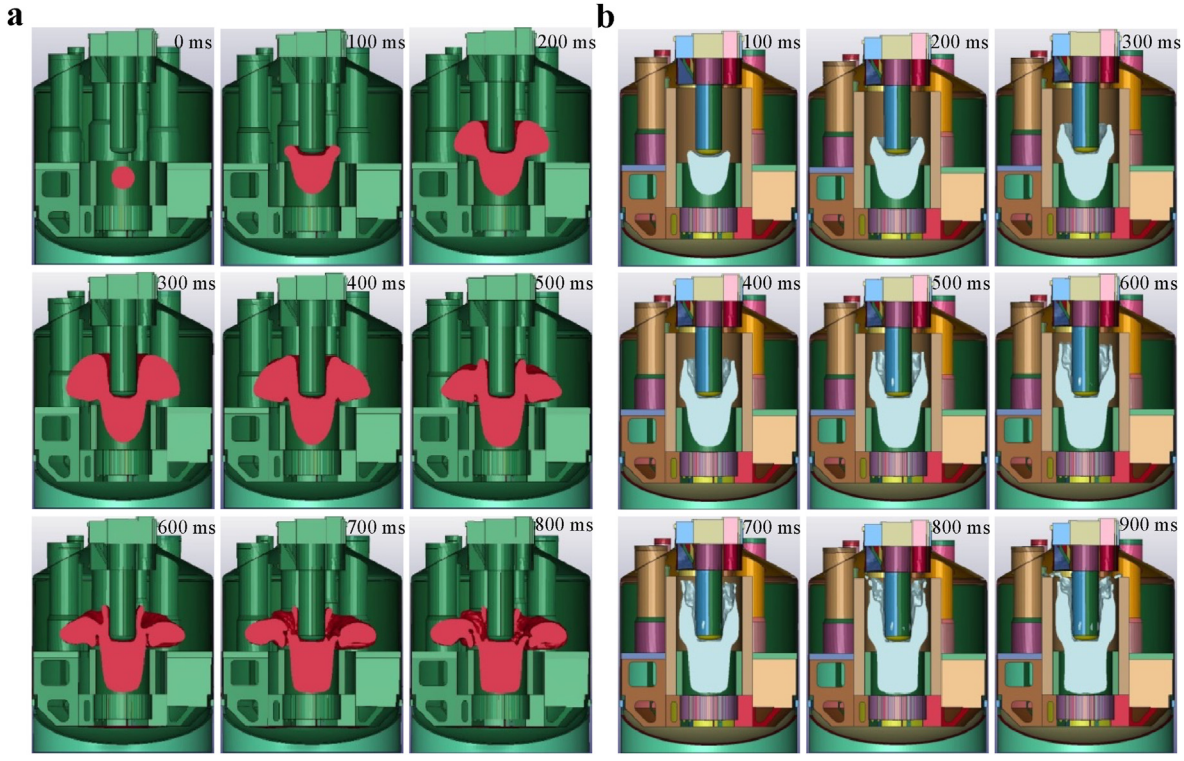

Fig. 9. Expansion dynamics of gas core for models without (a) and with (b) heat shield under core energy of 100 MJ. Note that the color schemes of the two figures are not the same to highlight the existing of the heat shield. (For interpretation of the references to color in this figure legend, the reader is referred to the Web version of this article.)

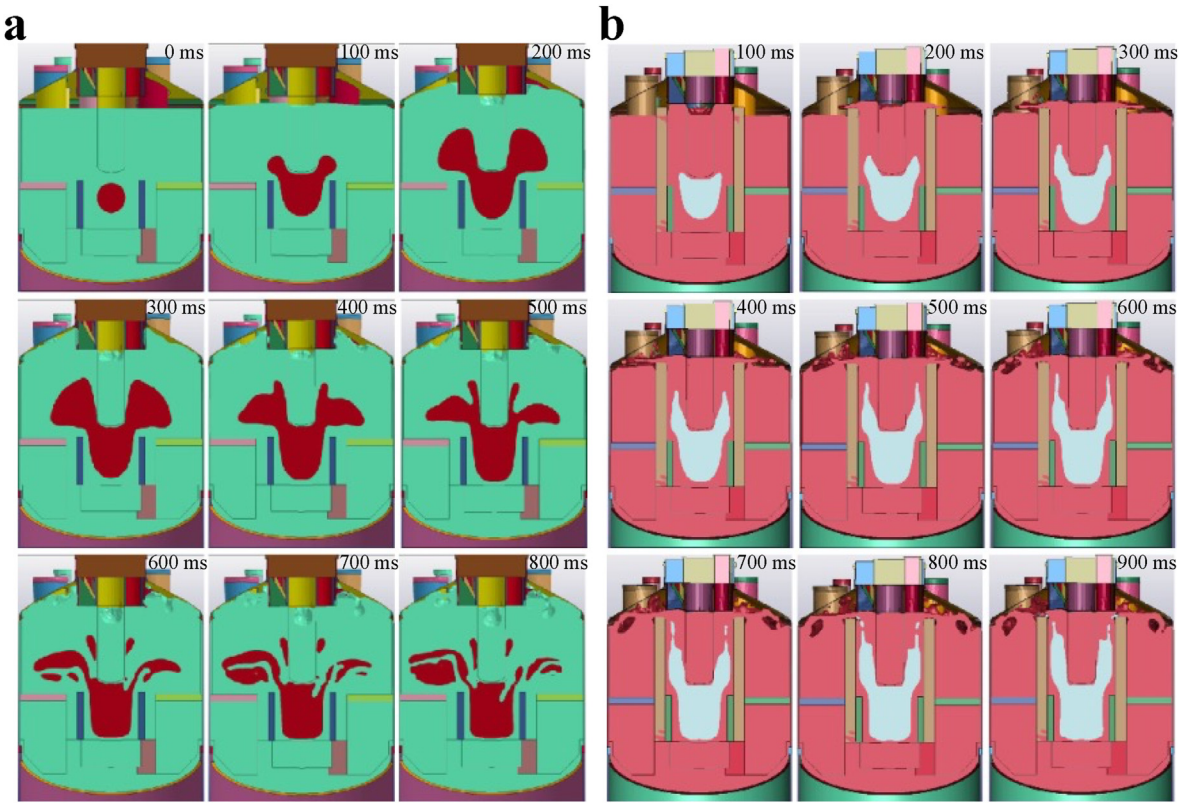

Fig. 10. Flow dynamics of liquid sodium under two cases of without (a) and with (b) heat shield under core energy of 100 MJ. In (a), liquid and sodium vapor are represented in green and red, respectively, while they are represented in pink and grey, respectively, in (b). (For interpretation of the references to color in this figure legend, the reader is referred to the Web version of this article.)

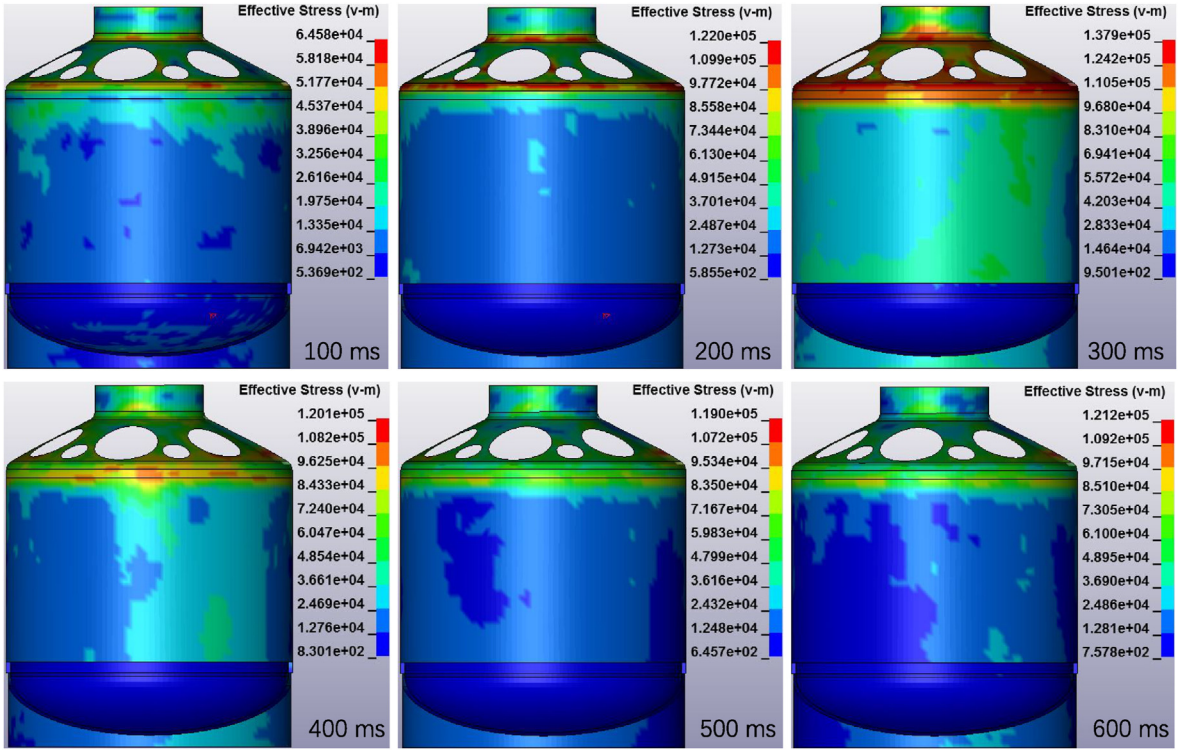

Fig. 11. Contour diagrams of effective stresses of main container for models without heat shield under core energy of 50 MJ.

Subsequently the interface is obstructed by the bottom surface of the plug. The interface deforms and rushes into the junction between the cone-top-cover and the plug at 300 ms. The interface declines with the retraction of the gas core from 400 ms to 800 ms. In the presence of the heat shield, as shown in Fig. 10b, the expansion of the gas core is reduced to push a smaller volume of sodium. In addition, owing to the confinement of the structures, liquid sodium flows horizontally out from the top of the head shield (as shown from 200 ms to 600 ms). Thus, sodium does not rush into the junction between the cone-top-cover and the plug.

3.3. Structural responses

The deformation or damage of the main container is an important factor that determines whether an entire reactor remains intact during the serious consequences of an HCDA. Fig. 11 shows the effective stress (or von Mises stress) contours of the main container for the models without the heat shield under the core energy of 50 MJ. It can be seen that the shoulder of the main container (between the conical top and the cylindrical body) suffers from the high stress during the HCDA. Concurrent, a large area of the conical top of the container experiences a strong impact at 300 ms.

Fig. 12 shows the time evolutions of the stress intensities at a few key positions that are determined from the stress contours. Each row of subplots shows the position of the grid element and the corresponding variations in the stress intensity for different simulation conditions (as labeled in the plots). Fig. 12a corresponds

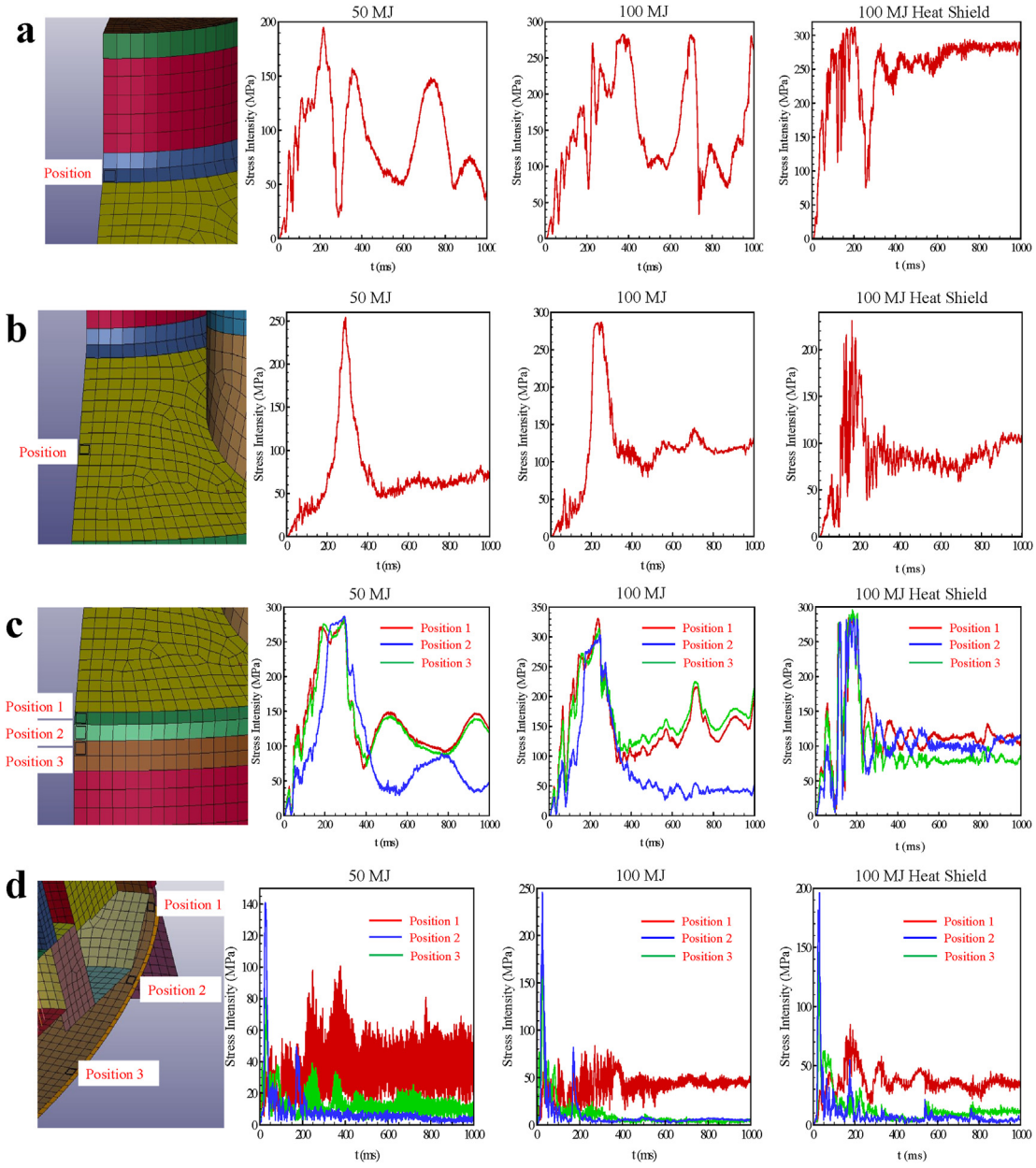

Fig. 12. Time evolution of stress intensity at key locations of container.

to a position at the upper boundary of the cone-top-cover. For the model without the heat shield, the stress intensity initially increases and subsequently oscillates. Understandably, the maximum value of the stress intensity is higher under 100 MJ than that under 50 MJ. Under the condition of the heat shield model under 100 MJ, the maximum value of the stress intensity is similar to that for the model without the heat shield. However, the stress intensity appears to equilibrate approximately after 400 ms. For a position at the middle of the cone-top-cover, as shown in Fig. 12b, major pulses are observed under the three conditions. Under the two conditions without the heat shield, both the maximum and equilibrium values of the stress intensity increase with the core energy. The maximum value for the model with the heat shield under 100 MJ is similar to that for the model without the heat shield under 50 MJ, indicating a

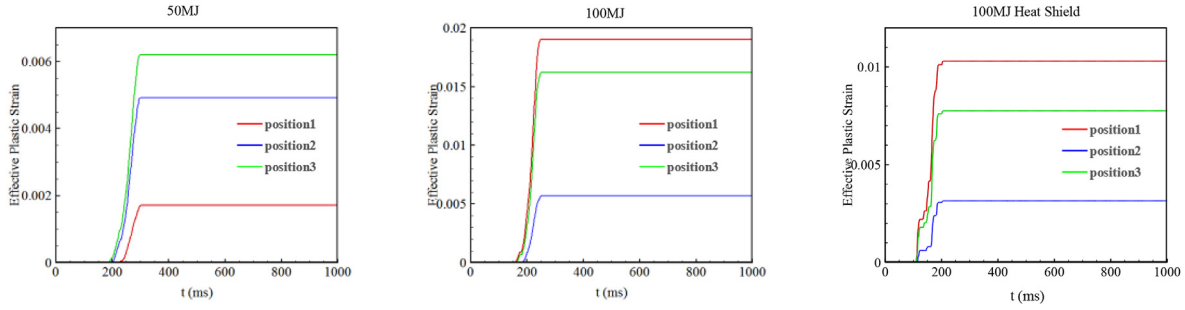

Fig. 13. Time evolutions of effective plastic strains at lower boundary of cone-top-cover.

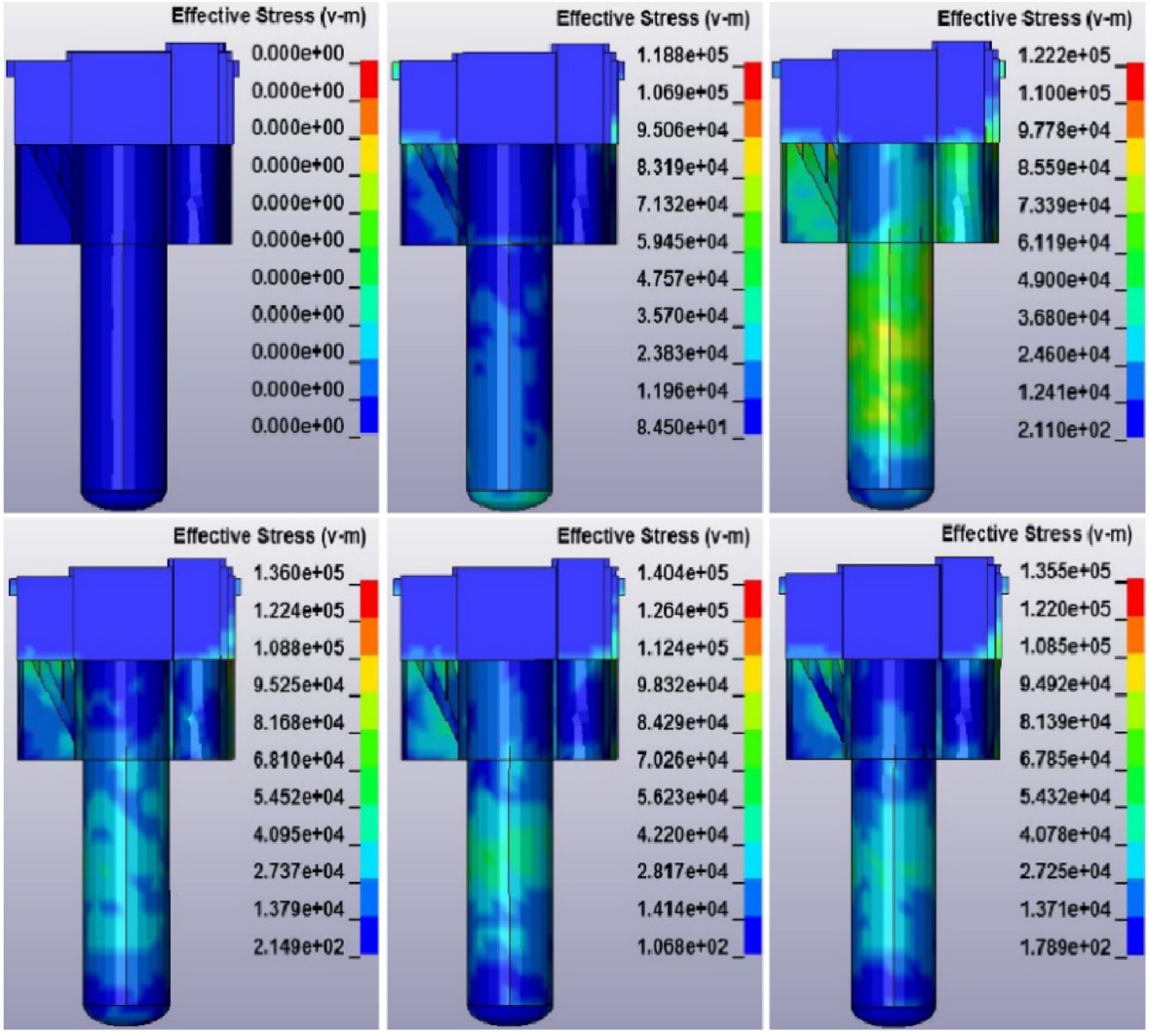

Fig. 14. Contour diagrams of effective stresses of separated plug for model without heat shield under core energy of 50 MJ.

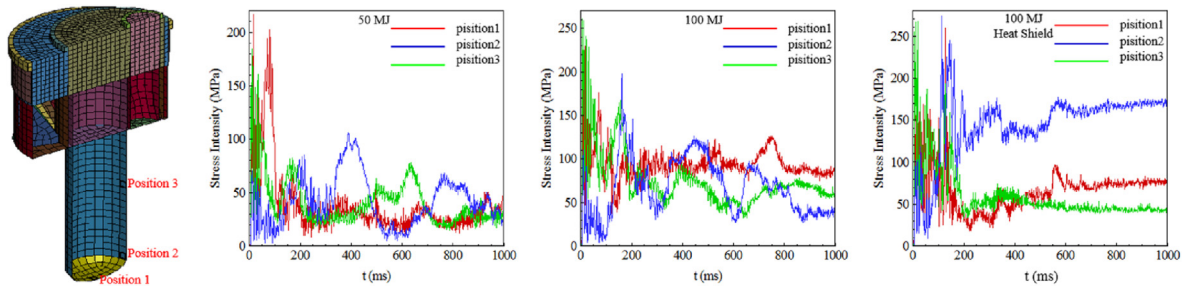

Fig. 15. Time evolutions of stress intensities at key locations of separated plug under different conditions: without heat shield under core energy of 50 MJ (a) and 100 MJ (b), and with heat shield under core energy of 100 MJ (c).

protection effect of the heat shield. However, the equilibrium value of the stress intensity is almost the same under the two conditions under 100 MJ. Similar variations and comparisons are observed for locations at the lower boundary of the cone-top-cover (Fig. 12c) and bottom of the container (Fig. 12d). When comparing vertically the subplots in Fig. 12, the lower boundary experiences the strongest pulse during the HCDA. In addition, the stress intensities at all positions do not exceed 350 MPa, which is much less than the allowable stress of 316L steel (520 MPa) [40]. Combining the above stress intensity plots and the stress contour diagrams in Fig. 11, after the explosion begins, the main container is severely impacted, particularly the lower boundary of the cone-top-cover; however, the stress intensity of the entire container is within an acceptable range. Fig. 13 further shows the time evolutions of the effective plastic strains at the lower boundary of the cone-top-cover. It is found that the main container experiences small plastic deformations during the HCDA.

The response of the plug is another important factor because the plug is between the fluids in the container and the ambient. Fig. 14 shows the effective stress contours of the separated plug for model without the heat shield under the core energy of 50 MJ. It can be seen that the lower end of the plug suffers from a high stress during the early stage of the HCDA. Concurrently, a large area of high stress on the middle plug is observed at 300 ms.

Fig. 15 shows the time evolutions of the stress intensities at a few key positions that are determined from the stress contours under different conditions. For the two conditions without the heat shield, Fig. 15a and b shows that broadly, the stress intensity increases with the core energy in terms of both the maximum and quasi-stable values after 1000 ms. For the condition with the heat shield under a core energy of 100 MJ, Fig. 15c shows that the plug suffers a longer duration of high stress than under the other two conditions. This indicates that the presence of the heat shield has a significant influence on the structural responses of the plug. Fig. 16 further shows the corresponding time evolutions of the effective plastic strains at the above key locations. Consistent with the results in Fig. 15, the condition with the heat shield under a core energy of 100 MJ has maximum values at all key positions among the three conditions. The maximum effective plastic strain is used at position 1 with a value less than 0.004, indicating that the deformations are still acceptable.

3.4. Plug rises

The plug at the top of the container can rise during an HCDA, causing the opening of the leakage channels of the fluid inside the container. Thus, it is of major importance to evaluate the rising of the plug. For safety reasons, an integral plug without the tin–bismuth alloy sealing and a separated plug with the sealing are considered in the present study. The first condition is the worst

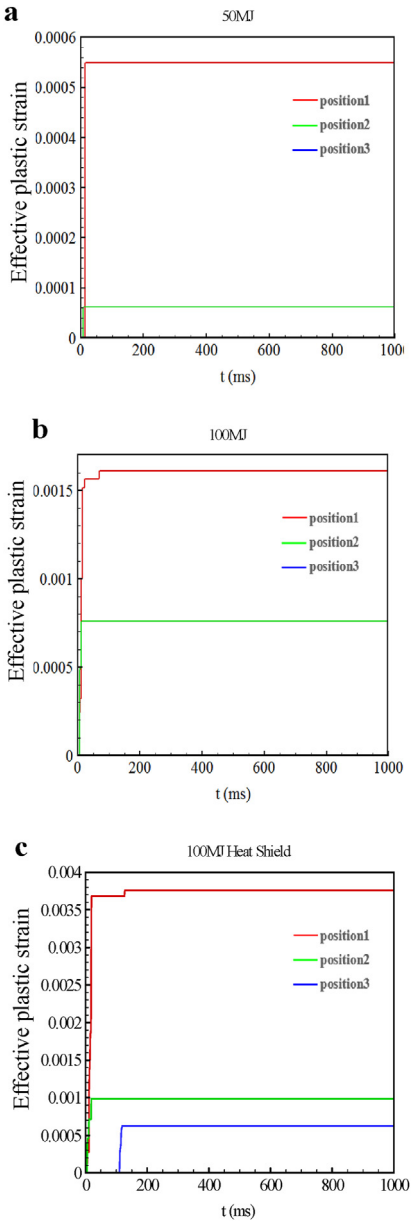

Fig. 16. Time evolutions of effective plastic strains at key locations of separated plug under different conditions. Note that position 2 has negligible value in (a) and (b) in comparison to other positions.

scenario because of the lack of resistance of the sealing. The second condition is more complex but is a more realistic scenario than the

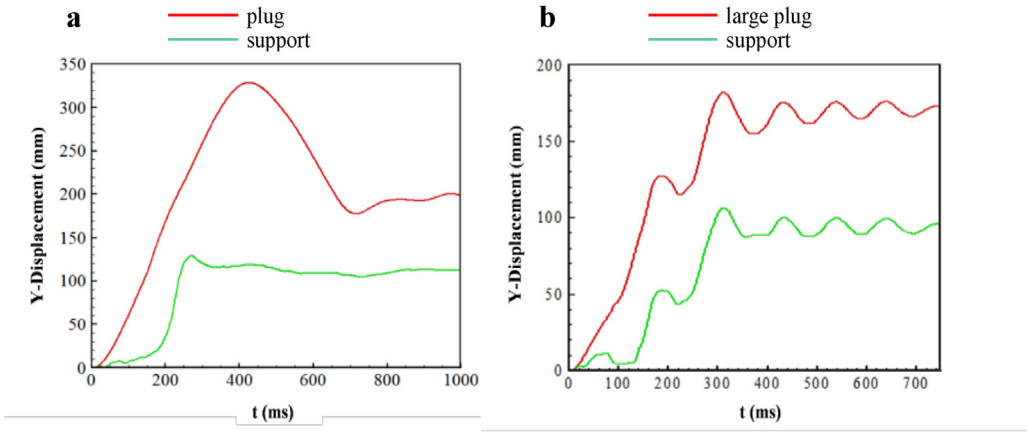

Fig. 17. Comparison of displacements of plug for models without heat shield under core energy of 100 MJ: (a) Integral plug and (b) Separated plug. Note that the displacement is represented by that of the large plug in (b).

first one. Fig. 17 compares the displacements of the large plug and its support in the vertical direction under the two conditions. Fig. 17a shows that in the first condition, the large plug initially rises and subsequently drops to a plateau, whereas the support first rises, subsequently slightly drops, and finally reaches a plateau. The relative displacement of the large plug and its support is approximately 80 mm after the pulse of the HCDA. Fig. 17b shows that under the second condition, both displacements first increase and subsequently reach plateaus in an oscillating pattern. The maximus displacement of the large plug is much smaller than that in Fig. 17a owing to the existence of the tin–bismuth alloy sealing. However, the relative displacements of the large plug and its support has similar values to those in the first condition.

Fig. 18 shows the vertical displacements of the large plug and its support for the models with the separated plug under different conditions. No separations are observed among the large, middle, and small plugs; therefore, the differences in the displacements of the three plugs can be excluded. This indicates that the HCDA does not destroy the tin–bismuth alloy connections among the three plugs. Comparing Fig. 18a and b shows that the displacements of the large plug and its support and the relative distance between them increase with the core energy. In the presence of the heat shield, Fig. 18c shows that the two displacements are longer than those in Fig. 18b for the same core energy without the heat shield. The relative displacement between the large plug and its support is approximately 200 mm, which is much larger than that in Fig. 18b. This is because the existence of the heat shield causes more core energy to transmit toward the plug, as already demonstrated in Fig. 10b.

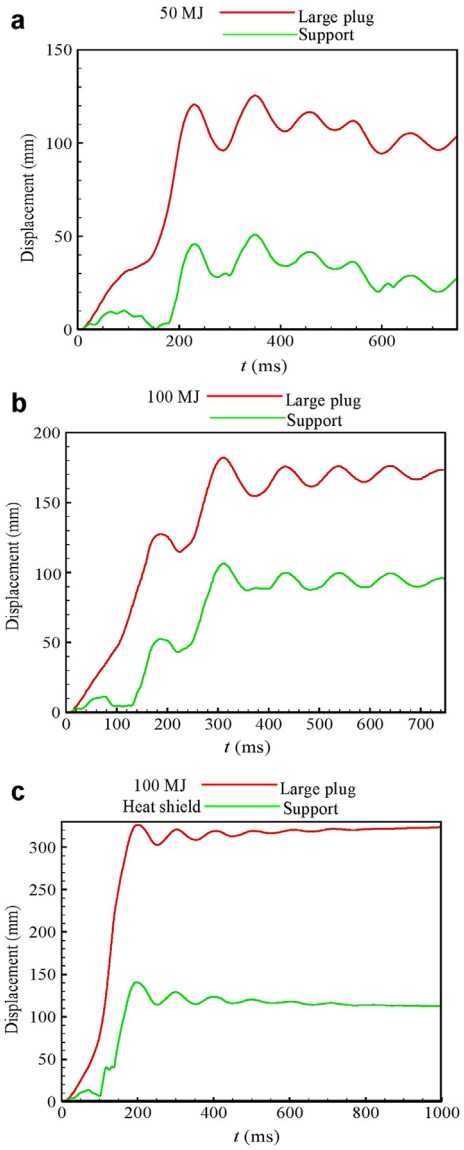

Fig. 18. Displacement of large plug and its support for models with separated plug: (a) Model without heat shield for core energy of 50 MJ, (b) Model without heat shield for core energy of 100 MJ, and (c) Model with heat shield for core energy of 100 MJ.

4. Conclusion

In this study, full-scale numerical simulations were conducted to investigate the interactions between the fluids and the structures in a sodium-cooled fast reactor during an HCDA. The physical model considered the main components that are influenced by the accident as well as the realistic interactions among the components. The MMALE method was selected to describe the fluids, whereas the Lagrangian method was used to describe the structures. The penalty function method was employed to treat the interactions between the fluids and the structures. The results showed that the maximum stress intensity experienced by the internal components of the reactor cannot exceed the allowable stress value for a core energy up to 100 MJ. However, the structural deformations are within the tolerable range, to ensure the integrity

of the container. During the accident, the tin–bismuth alloy sealing of both the large plug and its support were destroyed, causing the plug to rise but not escape. A separation distance of approximately 200 mm was observed between the large plug and its support under 100 MJ. Consequently, the leakage channels between the large plug and the container body became opened, allowing the fluid to drain. Expectedly, the boundary conditions at the entrance of the leakage channels can be obtained from the full-scale simulations to allow estimation of the leakage of liquid sodium.

Declaration of competing interest

The authors declare that they have no known competing financial interests or personal relationships that could have appeared to influence the work reported in this paper.

Acknowledgments

This study was partly supported by the National Natural Science Foundation of China (Grant No. 11772343) and the Beijing Institute of Technology Research Fund Program for Young Scholars.

References

[1] Z.T. Su, C.Y. Ye, F.W. Yan, Liquid-sodium Fast Breeder Reactor, Atomic Energy Press, Beijing, 1991 (in Chinese).
[2] T. Suzuki, T. Yoshiharu, K. Kenichi, et al., A preliminary evaluation of unprotected loss-of-flow accident for a prototype fast-breeder reactor, Nucl. Eng. Technol. 47 (3) (2015) 240–252.
[3] R.B. Nicholson, J.F. Jackson, A Sensitivity Study for Fast Reactor Disassembly Calculations. ANL-7952, 1974.
[4] H. Niwa, A comprehensive approach of reactor safety research aiming at elimination of recriticality in CDA for commercialization of LMFBR, Prog. Nucl. Energy 32 (3/4) (1998) 621–629.
[5] H.A. Bethe, J.H. Taite, An estimate of the order of magnitude of the explosion when the core of a fast reactor collapses, in: British Report UKAEA-RHM (56)/113, 1956.
[6] R.B. Nicholson, J.F. Jackson, VENUS-11: an LMFBR Disassembly Program, Argonne National Laboratory ANL, USA, 1972, p. 7952.
[7] T. Suzuki, K. Kamiyama, H. Yamano, et al., A scenario of core disruptive accident for Japan sodium-cooled fast reactor to achieve in-vessel retention, J. Nucl. Sci. Technol. 51 (4) (2014) 493–513.
[8] A.M. Tentner, Severe Accident Approach – Final Report Evaluation of Design Measures for Severe Accident Prevention and Consequence Mitigation, Argonne National Laboratory, Nuclear Engineering Division, 2010. http://www.osti.gov/bridge.
[9] M.F. Robbe, M. Lepareux, E. Treille, et al., Numerical simulation of a hypothetical core disruptive accident in a small-scale model of a nuclear reactor, Nucl. Eng. Des. 223 (2) (2003) 159–196.
[10] H. Yamano, S. Kubo, Y. Shimakawa, et al., Safety design and evaluation in a large-scale Japan sodium-cooled fast reactor, in: Science and technology of nuclear installation (PT.2):614973.1-61614973.14, 2012.
[11] Y.W. Chang, Analysis of HCDA, Nucl. Eng. Des. 69 (1982) 345–358.
[12] P.H. West, N.E. Hoskin, Suggested simple test problems for examination of thin shell modelling and fluid structure coupling, in: Aldermaston Report AWRE/44/92/16, APRICOT—phase, 1980, p. 3.
[13] K.C. Kendall, D.J. Adnams, Experiments to Validate Structural Dynamics Code Used in Fast Reactor Safety Assessment. Science and Technology of Fast Reactor Safety, British Nuclear Energy Society, London, UK, 1986.
[14] M. Falgayrettes, C. Fiche, P. Granet, et al., Response of a 1/20 scale mock-up of the Superphenix breeder reactor to an HCDA loading simulation, in: Proceedings of the Seventh International Conference on Structural Mechanics in Reactor Technology, 1983, pp. 157–166. Paper E 4/1, Chicago, USA.
[15] R.J. Tobin, D.J. Cagliostro, D.W. Ploeger, Energetics of simulated HCDA bubble expansions: some potential attenuation mechanisms, Nucl. Eng. Des. 58 (1) (1979) 85–95.
[16] I.G. Cameron, B.C. Hankin, A.G.P. Warham, A. Benuzzi, A. Yerkess, The computer code SEURBNUK-2 for fast reactor explosion containment safety studies, in: Proceedings of the Fourth International Conference on Structural Mechanics in Reactor Technology, 1977. Paper B 2/1, San Francisco, USA.
[17] B.L. Smith, A. Yerkess, J. Adamson, Status of coupled fluid-structure dynamics code SEURBNUK, in: Proceedings of the Seventh International Conference on Structural Mechanics in Reactor Technology, 1983. Paper B 9/1, Chicago, USA.
[18] M. Cigarini, A. Daneri, G. Toselli, Applications of ASTARTE-4 code to explosive models with complex internal structure using the rezoning facility, in: Proceedings of the Seventh International Conference on Structural Mechanics in Reactor Technology, 1983. Paper B 9/3, Chicago, USA.
[19] J.L. Graveleau, P. Louvet, Calculation of fluid-structure interaction for reactor safety with the CASSIOPEE code, in: Proceedings of the Fifth International Conference on Structural Mechanics in Reactor Technology, 1979. Paper B 1/7, Berlin, Germany.
[20] Y. Blanchet, P. Obry, J. Louvet, Treatment of fluid-structure interaction with the SIRIUS computer code, in: Proceedings of the Sixth International Conference on Structural Mechanics in Reactor Technology, 1981. Paper B 8/8, Paris, France.
[21] M. Lepareux, H. Bung, A. Combescure, J. Aguilar, J.F. Flober, Analysis of an HCDA in a fast reactor with a multiphase and multicomponent behavior law, in: Proceedings of the 12th International Conference on Structural Mechanics in Reactor Integrity, 1993, pp. 197–202. Paper E 7/2, Stuttgart, Germany, August.
[22] Y. Cariou, J.P. Pirus, C. Avallet, LMR large accident analysis method, in: Proceedings of the 14th International Conference on Structural Mechanics in Reactor Technology, 1997, pp. 395–402. Paper P 3/7, Lyon, France, August.
[23] M.F. Robbe, M. Lepareux, E. Treille, Estimation of the mechanical effects of a core disruptive accident on a LMFBR, in: International Conference on Nuclear Engineering, Nice, Acropolis (France), 2001, pp. 8–12. April.
[24] M.F. Robbe, M. Lepareux, E. Treille, et al., Numerical simulation of an explosion in a simple scale model of a nuclear reactor, Comput. Assist. Mech. Eng. Sci. 9 (4) (2002) 489–517.
[25] M.F. Robbe, M. Lepareux, Y. Cariou, Numerical interpretation of the MARA 8 experiment simulating a hypothetical core disruptive accident, Nucl. Eng. Des. 220 (2) (2003) 119–158.
[26] M.F. Robbe, M. Lepareux, E. Seinturier, Computation of a core disruptive accident in the MARS mock-up, Nucl. Eng. Des. 235 (13) (2005) 1403–1440.
[27] V. Faucher, P. Galon, A. Beccantini, et al., Hybrid parallel strategy for the simulation of fast transient accidental situations at reactor scale, in: International Conference on Supercomputing in Nuclear Applications, Monte Carlo, 2013.
[28] J.L. Yang, X.J. Cai, C.H. Wu, Experimental and FEM study of windshield subjected to high speed bird impact, Acta Mech. Sin. 19 (6) (2003) 543–550.
[29] H.C. Huang, et al., Thermal Technology Dictionary, vol. 467, Shanghai Lexicographical Publishing House, 1996.
[30] L.E. Felton, C.H. Raeder, D.B. Knorr, The properties of tin-bismuth alloy solders, JOM (J. Occup. Med.) 45 (7) (1993) 28–32.
[31] D.J. Benson, A mixture theory for contact in multi-material Eulerian formulations, Comput. Methods Appl. Mech. Eng. 140 (1) (1997).
[32] G. Barras, M. Souli, N. Aquelet, et al., Numerical simulation of underwater explosions using an ALE method. The pulsating bubble phenomena, Ocean Eng. 41 (2012) 53–66.
[33] M. Souli, A. Ouahsine, L. Lewin, ALE formulation for fluid-structure interaction problems, Comput. Methods Appl. Mech. Eng. 190 (2000) 659–675.
[34] H. Zhao, et al., LS-DYNA Dynamic Analysis Guide, Ordnance Industry Press, 2003 (in Chinese).
[35] J.H. Ding, X.L. Jin, G.G. Li, et al., Three-dimensional cutting simulation by cutterhead of shield machine based on parallel computing, J. Syst. Simul. 19 (23) (2007), 5376-5375.
[36] X.J. Wang, Z. Zong, Y. Zhao, et al., A numerical study of passenger side airbag deployment based on arbitrary Lagrangian-Eulerian method, Sci. China Technol. Sci. 58 (3) (2015) 397–404.
[37] ASME Boiler & Pressure Vessel Code. II Materials, Part D. Properties, 2015.
[38] O.H. John, LS-DYNA Theoretical Manual, Livermore Software Technology Corporation, 2018.
[39] A. Benuzzi, Comparison of different LMFBR primary containment codes applied to a benchmark problem, Nucl. Eng. Des. 100 (2) (1987) 239–249.
[40] China Iron and Steel Industry Association, GB/T 5216-2014 Structural Steels with Specified Hardenability Bands, Standards Press of China, Bei Jing, 2014.